

On cooperative instabilities of parallel vortex pairs

By R. L. BRISTOL, J. M. ORTEGA, P. S. MARCUS
AND Ö. SAVAŞ

Department of Mechanical Engineering, University of California at Berkeley,
Berkeley, CA 94720-1740, USA
savas@me.berkeley.edu

(Received 11 February 2003 and in revised form 24 June 2004)

We present a combined analytical and numerical study of the instabilities of a pair of parallel unequal-strength vortices. We extend the analyses of a vortex in an external strain field (Crow, *AIAA J.* vol. 8, 1970, p. 2172; Widnall *et al.*, *J. Fluid Mech.* vol. 66, 1974, p. 35) to include the orbital motion of the vortex pair. For counter-rotating pairs, the classic Crow-type periodic displacement perturbations are unstable for all vortex strength ratios, with fastest-growing wavelengths several times the vortex spacing. For co-rotating pairs, the orbital motion acts to suppress instability due to displacement perturbations. Instabilities in this case arise for elliptic perturbations at wavelengths that scale with the vortex core size. We also examine the influence of a second vortex pair by extending Crouch's (*J. Fluid Mech.* vol. 350, 1997, p. 311) analysis. Numerical results from a spectral initial-value code with subgrid-scale modelling agree with the growth rates from the theoretical models. Computations reveal the nonlinear evolution at late times, including wrapping and ring-rejection behaviour observed in experiments. A pair of co-rotating Gaussian vortices perturbed by noise develops elliptic instabilities, leading to the formation of vorticity bridges between the two vortices. The bridging is a prelude to vortex merger. Analytic, computational and experimental results agree well at circulation Reynolds numbers of order 10^5 .

1. Introduction

Figure 1 shows trailing wake vortices of a large aircraft flying at its cruising altitude. Water entrained in their cores makes them visible. Photograph (a) shows hints of both long- and short-wave instabilities, which become clearly visible in photograph (b). In photograph (c), the long-wave instabilities are about to cross-link to form rings. There is no obvious evidence that the short-wave instabilities are important in the linking process. While the short wavelength modes seem not to affect the long ones, the opposite is not true. Leweke & Williamson (1998) showed that the amplitude of the short-wavelength modes was much greater near the portions of the vortices that were about to link, although this is not obvious in figure 1. The long-wave disturbances grow in the imposed strain field of each vortex acting on the other. Their wavelengths are several times the vortex separation (Crow 1970). In the high-wavenumber limit, the stability analysis can be simplified by assuming that the strain field experienced by each vortex remains unaltered by the instability arising on the partner vortex; hence, the perturbations de-couple (Tsai & Widnall 1976). The resulting model illustrates

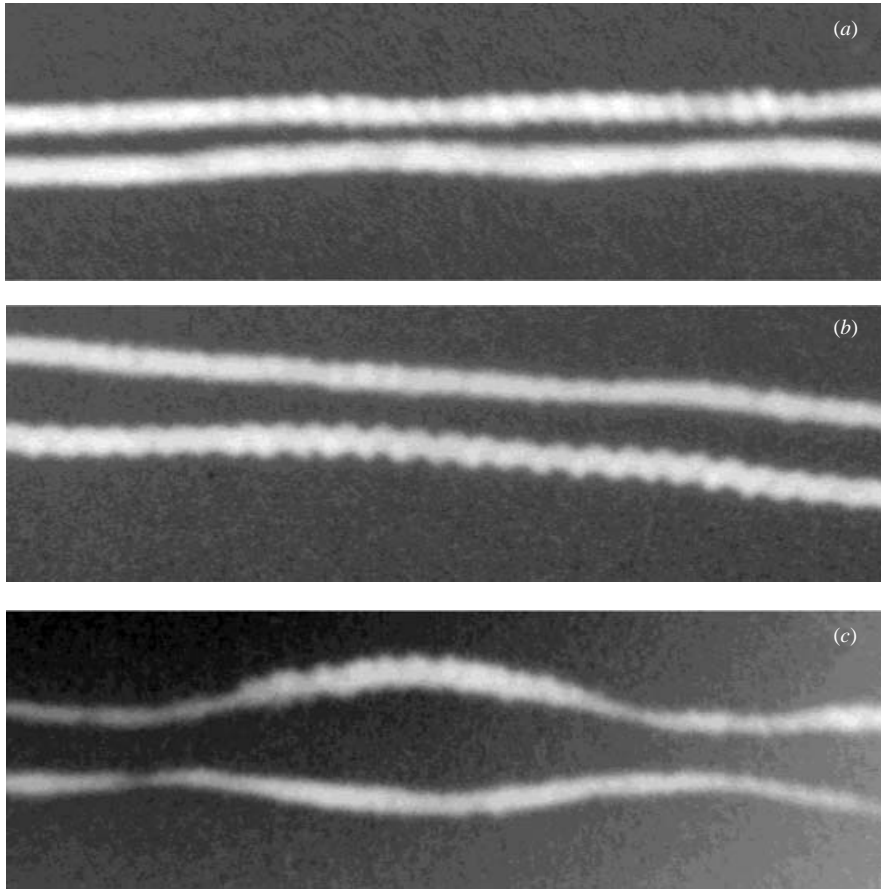


FIGURE 1. Photographs of an airplane wake in cruise, showing simultaneous long- and short-wave instabilities on trailing vortices. The photographs are taken at ground level with a 400 mm telephoto lens.

the competition between the self-induced rotation of the plane of the perturbation and the destabilization due to the strain field. Standing, opposing helical Kelvin waves sum to yield a planar wave that grows in the strain field. These displacement perturbations yield the instability considered by Crow. Short-wave elliptic instabilities can have resonance in the strain field. Moore & Saffman's (1975) and Tsai & Widnall (1976)'s more sophisticated analyses of Rankine (uniform core) vortices followed Crow's work. These studies took into account the strained, elliptical, two-dimensional cross-section of the vortex. The growth rate of the three-dimensional instability is greater than the strength of the imposed strain field. This growth enhancement is brought about by an additional internal strain field due to the elliptic shape of the perturbed vortex. Similar instabilities have been found in two-dimensional flows with elliptic streamlines (Bayly 1986; Pierrehumbert 1986). Eloy & Le Dizes (1999) have solved for the behaviour of instabilities of a Gaussian vortex in a weak strain field. Leweke & Williamson (1998) have made experimental observations of short-wave instabilities on a closely spaced vortex pair of equal strength and opposite rotation at Reynolds numbers of about 3000. They directly confirm the elliptic instability using flow visualization and particle image velocimetry (PIV), although the wavenumbers

were less than those predicted by Eloy & Le Dizès (1999). A review of the elliptical instability may be found in Kerswell (2002).

Jimenez (1975) has applied Crow's linear instability analysis to the case of equal-strength co-rotating vortices, finding them to be stable to long-wave displacement perturbations. Including some nonlinear effects, Klein, Majda & Damodaran (1995) confirmed a counter-rotating pair to be unstable, but did not find instabilities for co-rotating vortex pairs. More recently, Le Dizès & Laporte (2002) have extended their earlier work (Eloy & Le Dizès 1999) to the problem of elliptical instabilities arising in strained Gaussian vortex pairs, even accounting for the effect of Reynolds number.

This paper provides an explanation for the initial appearance of the sinuous instabilities observed in our recent experiments on co- and counter-rotating vortex pairs (Bristol 2000; Ortega 2001; Ortega & Savaş 2001). Samples of co-rotating vortex pair behaviour are shown in figure 2(*a, b*) and counter-rotating vortex pair behaviour in figure 2(*c*), where vortices are marked by dye released into their cores. The merger of co-rotating vortices in figure 2(*a, b*) is preceded by the appearance of growing, sinuous disturbances on each vortex, with a wavelength several times the core size of the vortex (Chen, Jacob & Savaş 1999; Bristol, Ortega & Savaş 1999, 2003). Much more pronounced sinuous disturbances are observed in the case of the counter-rotating vortex pairs in figure 2(*c*). The wavelength is several times the separation of the vortices. Instead of simply merging, the weaker vortex wraps around the stronger one, eventually forming periodic loops, which pinch off to form vortex rings (Ortega, Bristol & Savaş 2003). An extension of the linear instability analyses of Crow (1970) and Tsai & Widnall (1976) that accounts for the orbiting unperturbed state of the vortex pair successfully explains our observations. The more rigorous methods of Le Dizès & Laporte (2002) and Klein *et al.* (1995) (for the long-wavelength modes) could be used as alternative methods. Fabre, Jacquin & Loof (2002) have recently carried out a thorough calculation of the evolution of displacement disturbances on a four-vortex system consisting of two symmetric pairs of counter-rotating vortices, which shows remarkable agreement our observations. Despite its simplicity, however, the present work captures the essential physics of the instabilities. The eventual fate of the instability is investigated numerically using an initial value spectral code (Matsushima & Marcus 1997). Particular attention is paid to the events which trigger the occurrence of merger in the co-rotating case and the formation of loops in the counter-rotating case. We note that such loops have also been seen in the CFD results by Marshall, Brancher & Giovannini (2001), although at lower Reynolds numbers than the cases discussed here. Recently, Haverkamp, Neuworth & Jacob (2003) have presented results that aim at reproducing and explaining our experiments independently.

2. Linear instability of a parallel vortex-filament pair revisited

The analyses of Crow (1970), Widnall, Bliss & Tsai (1974) and Jimenez (1975) are extended to vortex pairs of arbitrary relative strength by including in the governing stability equations a term accounting for the orbital motion of the vortex pair. The circulation of the vortices is denoted by Γ_1 and Γ_2 . Γ_1 is the stronger vortex: $|\Gamma_1| \geq |\Gamma_2|$. The core radii are denoted by a_1 and a_2 , and are assumed to be small compared to their separation d (figure 3). In §2.1, we shall apply these core radii to both Rankine and Gaussian vorticity distributions. A right-handed

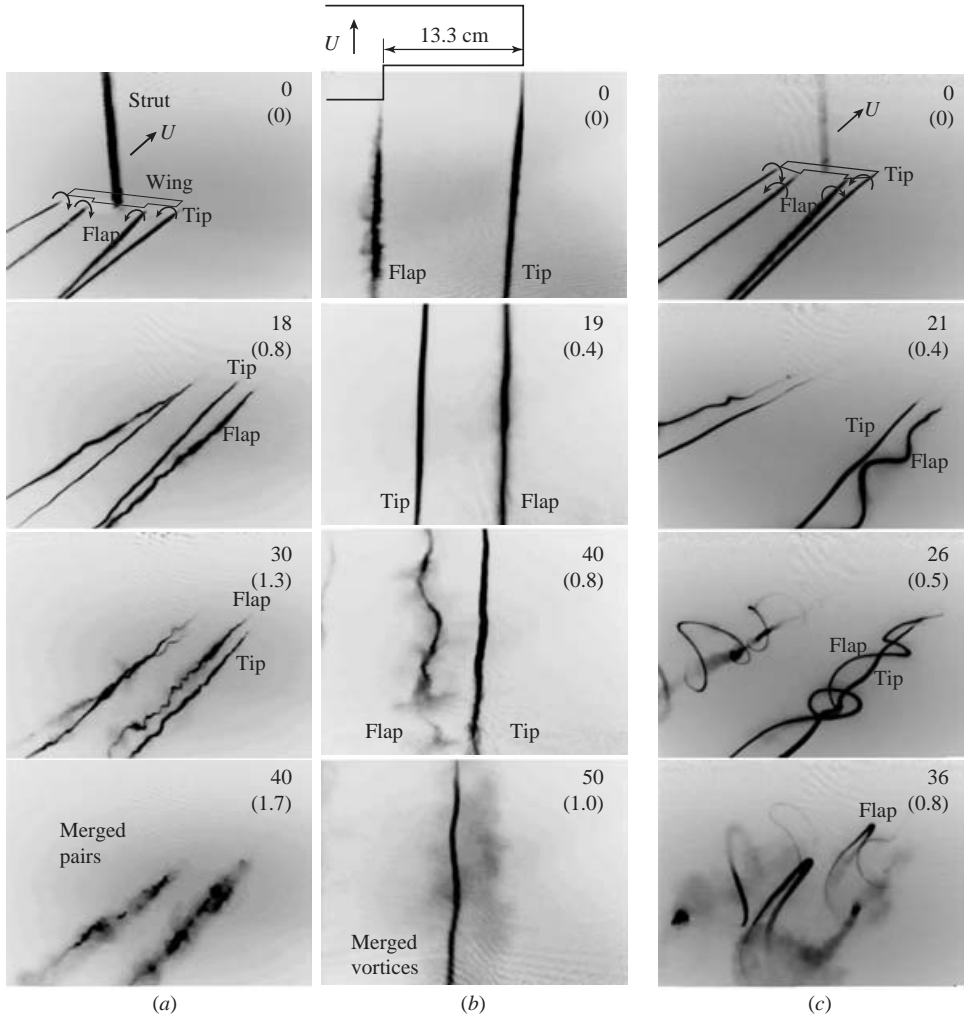


FIGURE 2. Dye visualization, inverted images are shown. Frames are labelled in terms of Ut/b and (t/T) ; U is the towing velocity, t the elapsed time since the wing left the view, b the wing span, and T the orbital period defined in equation (2.4) ($U = 500 \text{ cm s}^{-1}$, $b = 40 \text{ cm}$). (a) Two symmetric co-rotating vortex pairs in the wake of an in-board 50% flapped wing with $\Gamma = 1.0$, $d/\sigma = 5.0$, and $T \approx 1.88 \text{ s}$ (Bristol 2000). The frames show the formation of the vortex wake, appearance of the instability, and the final merged state. (b) Similar stages from an overhead, zoomed-in view of a $\Gamma = 0.9$, $d/\sigma = 6.67$, and $T \approx 3.88 \text{ s}$ pair off a 33% flapped wing. Note that the vortex pair has rotated about one revolution at $Ut/b = 40$. (c) Two symmetric counter-rotating vortex pairs in the wake of an out-board triangular flapped wing (Ortega 2001). Shown are stages of initial growth, formation of rings, and the crossover of these rings. $\Gamma = -0.37$, $d/\sigma_{tip} = 4$, $d/\sigma_{flap} = 7.3$, and $T \approx 3.80 \text{ s}$.

coordinate system (x, y, z) with unit vectors $(\mathbf{e}_x, \mathbf{e}_y, \mathbf{e}_z)$ is chosen such that \mathbf{e}_x is aligned with Γ_1 , and \mathbf{e}_y is in the initial plane of the vortex pair, hence, $\Gamma_1 > 0$. As in Crow (1970), each vortex is modelled as a filament; the internal structure is ignored, except for the effects of self-induction. In §4, we will investigate some of the effects of this approximation by comparing the results from numerical calculations.

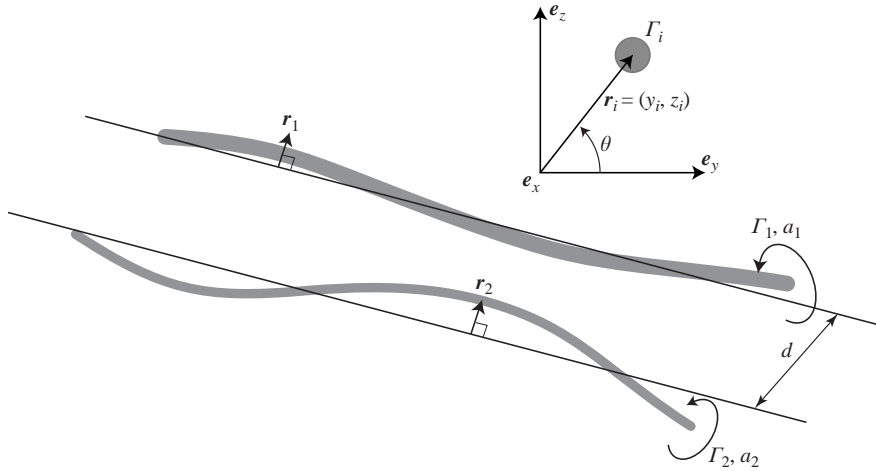


FIGURE 3. Definition of parameters used in the vortex filament model. Γ_i is the circulation, a_i the core size, and d the undisturbed vortex separation. Radial perturbations $\mathbf{r}_i = (y_i, z_i)$ are measured from the undisturbed position of vortices ($i = 1, 2$).

The parameter Γ is chosen to be the circulation ratio of the pair,

$$\Gamma \equiv \frac{\Gamma_2}{\Gamma_1}, \tag{2.1}$$

so that $-1 \leq \Gamma \leq 1$. We define a time scale

$$\tau = \frac{2\pi d^2}{\Gamma_1}, \tag{2.2}$$

which is the inverse of the strength of the strain field due to vortex Γ_1 acting at the separation distance d . Initially, the two vortices orbit about their vorticity centroid at the angular rate

$$\Omega = \frac{1 + \Gamma}{\tau}. \tag{2.3}$$

The orbital period is thus

$$T = \frac{2\pi \tau}{(1 + \Gamma)}. \tag{2.4}$$

When $\Gamma = -1$, the pair moves at a constant velocity of $-\mathbf{e}_z \Gamma_1 / 2\pi d$ and τ becomes the time for the pair to move a distance d . As in Crow, we prescribe on each vortex small radial displacement perturbations as Fourier modes, $\hat{\mathbf{r}}_i = \mathbf{r}_i \exp(st + ikx_i)$, where $\mathbf{r}_i = (y_i, z_i)$ are allowed to be complex, the wavenumber k is real, and s is the complex growth rate. Due to the symmetry of the problem, we need only consider $k > 0$. Indices are used to label vortices; no summation is implied unless explicitly indicated.

Following Crow's (1970) analysis, we write down the eigenvalue problem describing the evolution of the perturbations on the vortices as

$$\alpha \mathbf{y} = \mathbf{A} \mathbf{y} \tag{2.5}$$

where $\alpha = \tau s$, $\mathbf{y} = (y_1, z_1, y_2, z_2)^T$ and

$$\mathbf{A} = \underbrace{\begin{pmatrix} 0 & -\Gamma & 0 & 0 \\ -\Gamma & 0 & 0 & 0 \\ 0 & 0 & 0 & -1 \\ 0 & 0 & -1 & 0 \end{pmatrix}}_{\text{strain field}} + \underbrace{\begin{pmatrix} 0 & 0 & 0 & \Gamma\psi \\ 0 & 0 & \Gamma\chi & 0 \\ 0 & \psi & 0 & 0 \\ \chi & 0 & 0 & 0 \end{pmatrix}}_{\text{mutual induction}} \\ + \tau\Omega \underbrace{\begin{pmatrix} 0 & 1 & 0 & 0 \\ -1 & 0 & 0 & 0 \\ 0 & 0 & 0 & 1 \\ 0 & 0 & -1 & 0 \end{pmatrix}}_{\text{orbital rotation}} + \underbrace{\begin{pmatrix} 0 & \varpi_1 & 0 & 0 \\ -\varpi_1 & 0 & 0 & 0 \\ 0 & 0 & 0 & \Gamma\varpi_2 \\ 0 & 0 & -\Gamma\varpi_2 & 0 \end{pmatrix}}_{\text{self-induction}}.$$

The equation is written in the rotating reference frame of the vortex pair. The length scale is chosen as the unperturbed vortex separation d and the time scale is in units of τ ; χ and ψ are the mutual induction functions shown in Crow’s figure 4, which are composed of the modified Bessel functions of the second kind: $\chi(\beta) = \beta K_1(\beta)$ and $\psi(\beta) = \beta^2 K_0(\beta) + \beta K_1(\beta)$, where $\beta = kd$. Both $\chi(\beta)$ and $\psi(\beta)$ are equal to 1 at $\beta = 0$ and asymptote to 0 as $\beta \rightarrow \infty$. Note that $\tau\Omega = 1 + \Gamma$. ϖ_1 and ϖ_2 are the self-induced rotation rates of the vortices and are discussed in §2.1 below.

Let us consider the terms of the coefficient matrix \mathbf{A} . The first term represents the strain field from one vortex acting on perturbations on the other vortex. The second term represents the mutual induction between the vortices. For small values of β (long-wavelengths), ψ and χ are nearly equal to 1, yielding the purely two-dimensional effect that perturbations on one vortex essentially move the effective origin of the strain field imposed upon the other vortex. For finite values of β , the effect becomes three-dimensional in the sense that displacements all along vortices contribute. As β becomes much larger than one (short wavelengths), the perturbations on the vortices go through several cycles in an axial distance d , essentially averaging out and yielding small values of ψ and χ . Thus, the perturbations become decoupled in the high-wavenumber limit. The third and fourth terms serve to rotate the perturbations, due to the effect of orbit-induced rotation of the reference frame and self-induction, respectively. For the cases $\Gamma = -1$ and $\Gamma = +1$, the equations become equivalent to those derived by Crow (1970) and Jimenez (1975), respectively.

2.1. Self-induction of a vortex filament

In calculating the self-induction terms ϖ_i , we use Kelvin’s (1880) results for a uniform-core (Rankine) vortex and their extension to a Gaussian (Lamb–Oseen) vortex, rather than the cut-off approximation as was done in Crow (1970). As presented by Saffman (1992), the bending modes rotate with a constant angular velocity about the unperturbed axis at rates given by

$$\varpi_i^* = \frac{\Gamma_i}{2\pi a_i^2} \left(\frac{2k}{\sqrt{k^2 + \kappa_n^2}} - 1 \right), \tag{2.6}$$

where κ_n is the n th root from the dispersion relation (Saffman (1992), p. 232, equation 6), and is non-dimensionalized as

$$\varpi_i(k) = \beta^2 \frac{2\pi d^2}{\Gamma_i} \varpi_i^* \tag{2.7}$$

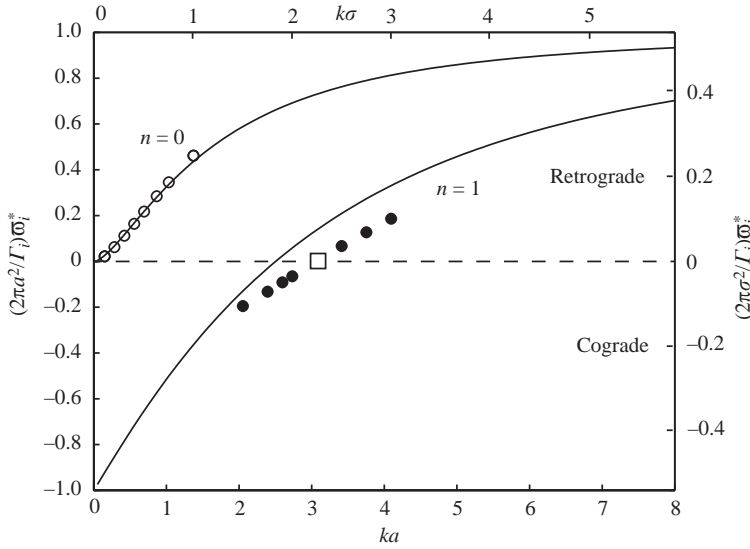


FIGURE 4. Vortex filament self-rotation rates for the modes with no radial node ($n=0$) and one radial node ($n=1$). The solid lines are for a Rankine vortex of circulation Γ_i and radius a (refer to the right and lower axes). The symbols are numerically calculated rotation rates for a Gaussian vortex of circulation Γ_i and dispersion radius $\sigma = 0.735a$ ($a = 1.36\sigma$) (refer to the left and upper axes). \circ , \bullet , Present calculations; \square , from Eloy & Le Dizès (1999).

which includes explicit k^2 dependence. For retrograde rotation (opposite to the azimuthal velocity of the vortex) $\omega_i^* > 0$ and for cograde rotation $\omega_i^* < 0$. The first root, $n=0$, corresponds to displacement perturbations, which are retrograde. The second root, $n=1$, is for elliptic modes with one radial node, in which the centre and the periphery of the vortex are displaced in opposite directions. These modes can rotate in either direction, depending on the value of ka_i . The rotation rates for the first two modes are shown as solid lines in figure 4. For $n \geq 1$, an additional cograde branch exists, for which $\omega_i^* < \Gamma_i/2\pi a_i^2$ for all k . However, these do not meet the criteria for instability as they self-rotate too quickly and will not be considered further. As argued by Robinson & Saffman (1984), modes with increasingly large values of n are damped for real flows with viscosity and are thus deemed to be less important than the $n=0$ and $n=1$ modes. In addition, as computed recently by Sipp (2000), the $n=1$ modes do not have as great a capacity for growth as do the $n=0$ modes. Therefore, we focus on the lowest value of n which gives instability: $n=0$ for counter-rotating pairs ($-1 < \Gamma < 0$), and $n=1$ for co-rotating vortex pairs ($0 < \Gamma < 1$).

The experimental vortices exhibit a radial distribution of axial vorticity $\omega_x(r)$ that closely follows that of a Gaussian (Lamb–Oseen) vortex (see, for example, Chen *et al.* 1999):

$$\omega_x = \frac{\Gamma_i}{\pi\sigma_i^2} e^{-r^2/\sigma_i^2} \tag{2.8}$$

where σ_i is the vorticity dispersion radius. Widnall, Bliss & Zalay (1971) and Moore & Saffman (1975) have shown that for $ka_i \ll 1$, the $n=0$ self-induced rotation rate of a Gaussian vortex is the same as that of a Rankine vortex of size $a_i = 1.36\sigma_i$ with the same circulation. A numerical study using the code of §4 below shows that this result remains valid even for wavenumbers of order one ($n=0$ in figure 4). Also

shown in the figure are results for the $n = 1$ mode needed for $\Gamma > 1$. Eloy & Le Dizès (1999) have calculated $k\sigma_i = 2.26$ for zero self-induction. Figure 4 shows their result, additional calculations for the $n = 1$ mode, and those for $n = 0$ using the numerical procedure described in §4. In their calculations, Fabre *et al.* (2002) used the method developed by Fabre & Jacquin (2000) to calculate the self-induced rotation, which precludes spurious instabilities. More accurate means of calculating this curve are available in Plobeck (1974) and Le Dizès & Laporte (2002).

In figure 4 above and the remainder of this paper, unless noted otherwise, we take $a = a_1 = a_2$ and $\sigma = \sigma_1 = \sigma_2$, which also implies $\varpi = \varpi_1 = \varpi_2$. We do this simplification mainly for later comparison to experiments of Ortega *et al.* (2003) where all vortices have nearly the same size, and to a lesser extent, to simplify the discussion.

2.2. Non-coupled vortex filament analysis

Following Widnall *et al.* (1974), we now consider a planar sinusoidal perturbation imposed on a single vortex subject to the strain field of the undisturbed companion vortex. This is equivalent to dropping the mutual induction term of \mathbf{A} in equation (2.5), which is strictly valid for $d \gg a$. In polar coordinates, equation (2.5) written in terms of the perturbation amplitude $\mathbf{r}_i = (y_i, z_i) = (r_i, \theta_i)$ is given by

$$(\dot{r}_i, \dot{\theta}_i) = \frac{1}{\tau} \left(\underbrace{-r_i \left(\Gamma + 1 - \frac{\Gamma_i}{\Gamma_1} \right) \sin 2\theta_i, - \left(\Gamma + 1 - \frac{\Gamma_i}{\Gamma_1} \right) \cos 2\theta_i}_{\text{strain field}} + \underbrace{\tau \Omega + \frac{\Gamma_i}{\Gamma_1} \varpi}_{\text{rotation}} \right) \quad (2.9)$$

where the overdot denotes the time derivative. Setting $\Gamma_i = -\Gamma_1$ ($\Omega = 0$) gives the equations derived by Widnall *et al.* (1974). The trigonometric terms in equation (2.9) describe a stagnation flow of strength Γ for vortex Γ_1 and of strength 1 for vortex Γ_2 . The term $\tau \Omega + \varpi \Gamma_i / \Gamma_1$ rotates the perturbation vector by the orbital rotation of the reference frame and self-induction. The strain field acts to destabilize the perturbation by amplifying it along the principal extensional axis. The rotation terms act to stabilize the perturbation by rotating it through this extensional axis. Thus for a perturbation to grow without bound, it must remain fixed at some angle. This condition, $\dot{\theta}_i = 0$, can only occur if the magnitude of the azimuthal component of the strain field is less than that of the rotational terms. Comparing these two terms for $i = 2$ (which covers the general case as the weaker vortex will become unstable before the stronger), we obtain a necessary condition for instability:

$$-2 \leq \Gamma(1 + \varpi) \leq 0. \quad (2.10)$$

For displacement perturbations for which $\varpi > 0$, the inequality (2.10) implies instability only for counter-rotating vortex pairs ($\Gamma < 0$), and not for co-rotating pairs ($\Gamma > 0$). The same conclusion holds even if the perturbations on each vortex are allowed to couple, by altering the imposed strain fields (§2.3). In his analysis of the short-wave instability of a $\Gamma = 1$ pair, Wang (1998) deduced the instability condition in his equation (8), which is a special case of equation (2.10) above.

From the viewpoint of an inertial frame, for instability the perturbation on the weaker vortex must rotate in the same sense as the orbital motion of the pair in order to remain aligned in the strain field of the partner vortex. Self-induced rotation acts on displacement perturbations in a retrograde sense, that is, it rotates them in the opposite sense to the vortex's own velocity field. For a co-rotating pair, this is in exactly the wrong direction to maintain alignment with the strain field.

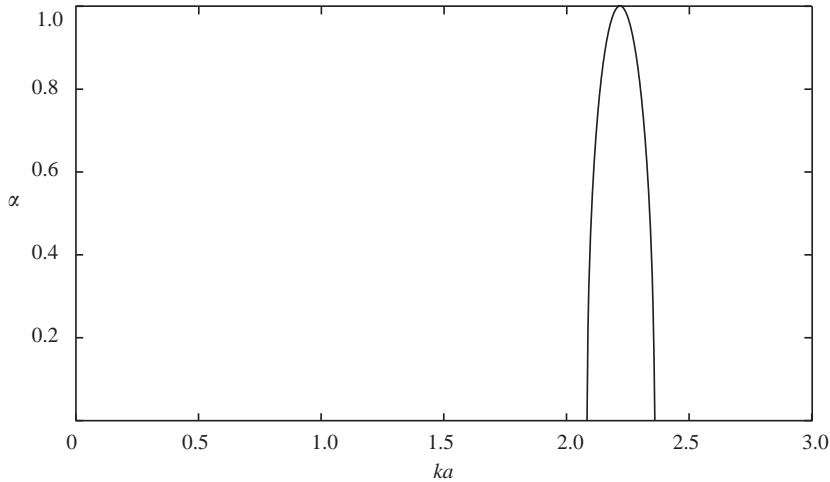


FIGURE 5. Growth rate α of the most unstable eigenvector for the $n = 1$ mode of co-rotating Rankine vortices ($\Gamma = 1$) with $d/a = 5$.

For instability in this case, we need a cgrade self-rotation. This is only possible for modes with internal structure ($n \geq 1$). For a counter-rotating vortex pair, the self-induced and orbit-induced rotations are in opposite directions for displacement perturbations. The two can thus balance each other and, hence, maintain alignment for rapid destabilization.

The $n = 1$ mode rotates in a cgrade sense ($\varpi_i < 0$) for $ka < 2.5$ for Rankine vortices (figure 4). Referring to equation (2.9), this can produce an exponential growth rate at $(ka)_{max}$ such that $\sin 2\theta_i = -1$ and $\theta_i = 0$, yielding the condition for maximum growth:

$$\varpi_i((ka)_{max}) = -\frac{1 + \Gamma}{\Gamma_i/\Gamma_1}. \tag{2.11}$$

Figure 5 shows the growth rate as a function of wavenumber for $\Gamma = 1$ and $d/a = 5.0$. A band of instability appears with a peak growth rate of 1 at $ka = 2.22$. The width of the band is 0.27.

2.3. Coupled vortex filament analysis

Figure 6 shows the growth rates of two pairs of co-rotating Gaussian vortices for two experimental cases calculated using the self-induced rotation rates $\varpi_i(k\sigma)$ from figure 4. As noted earlier, properly accounting for the internal structure of the elliptical instability would yield a maximum growth rate larger than 1. The wavenumber for maximum growth rate $(k\sigma)_{max}$ is 1.9 for the case $(\Gamma, d/\sigma) = (0.9, 6.67)$, and 1.7 for $(\Gamma, d/\sigma) = (1.0, 5)$. These same values are obtained using either the coupled (equation (2.5)) or uncoupled (equation (2.11)) models, since the corresponding values of kd (13 and 8.5) are high enough to effectively decouple the perturbations on the vortices.

Figure 7 shows growth rates as a function of wavenumber for vortex pairs of $\Gamma = -1.0, -0.5,$ and -0.25 . The self-induced rotation rate is based on the displacement modes ($n = 0$) using equation (2.6). The vortex size-to-separation ratio for both vortices is fixed at $a/d = 0.32$, which is equivalent to the cut-off distance to separation ratio of 0.2 used in the top plot of figure 9 in Crow's paper. In agreement with Crow, the maximum growth rate for $\Gamma = -1$ is approximately 0.8 at $kd \approx 1$.

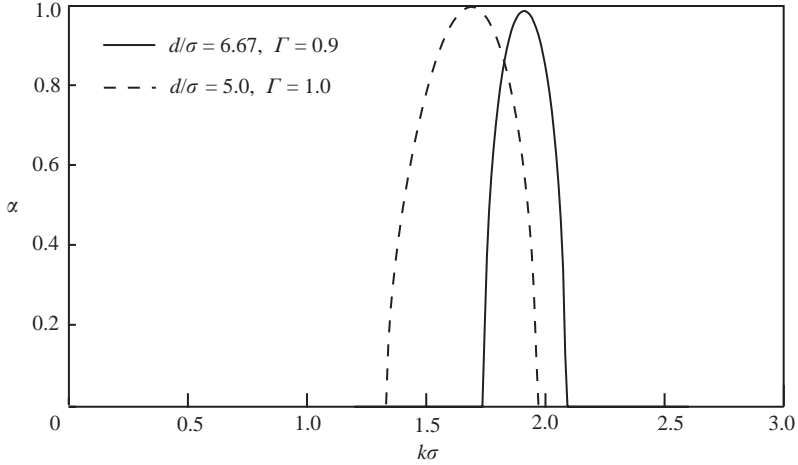


FIGURE 6. Growth rates α for co-rotating Gaussian vortex pairs using the numerically determined elliptic dispersion relation ($n = 1$) shown as ● in figure 4.

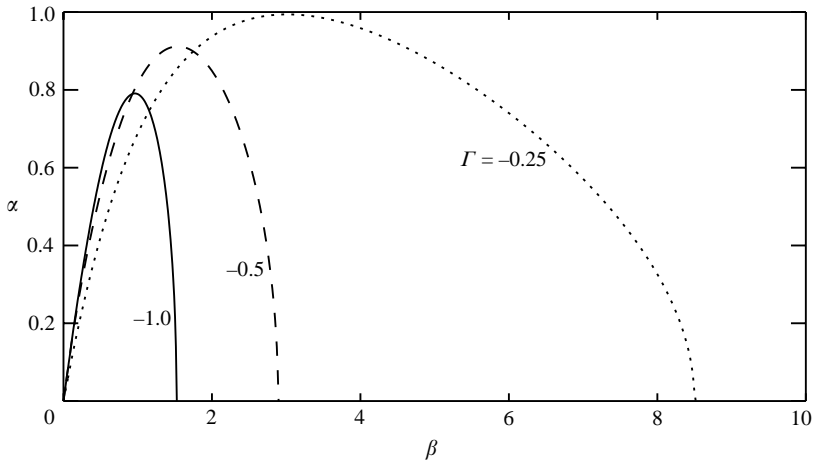


FIGURE 7. Growth rate α versus wavenumber β for displacement perturbations ($n = 0$) for three negative values of Γ and $a/d = 0.32$ (counter-rotating vortex pairs).

The smaller $|\Gamma|$ produce qualitatively similar results, but with a broader range of wavenumbers. Notably, the most unstable wavenumber increases as Γ approaches zero, which is consistent with the observations of Ortega *et al.* (2003). For the weaker vortex to balance the faster orbital rotation (for maximum growth), it must self-rotate at a higher rate, hence a higher wavenumber. From equation (2.11), as $\Gamma \rightarrow 0^-$, $\varpi_{max} \rightarrow -\Gamma^{-1}$. Considering the scaling of ϖ in equation (2.7), and equation (2.6) (or, equivalently, figure 4), we conclude that $kd \gg 1$ as $\Gamma \rightarrow 0^-$ for the most amplified wavenumbers.

A summary of the solution of the eigenvalue problem in equation (2.5) is shown in figure 8 for $-1 \leq \Gamma \leq 1$ and $0 \leq a/d \leq 0.5$ for displacement perturbations ($n = 0$). The maximum growth rate α_{max} is shown in figure 8(a) and the corresponding wavenumber β_{max} in figure 8(b). The growth rate α_{max} depends more strongly on Γ than a/d . As Γ increases from -1 to 0 , the maximum growth rate decreases to a minimum and then

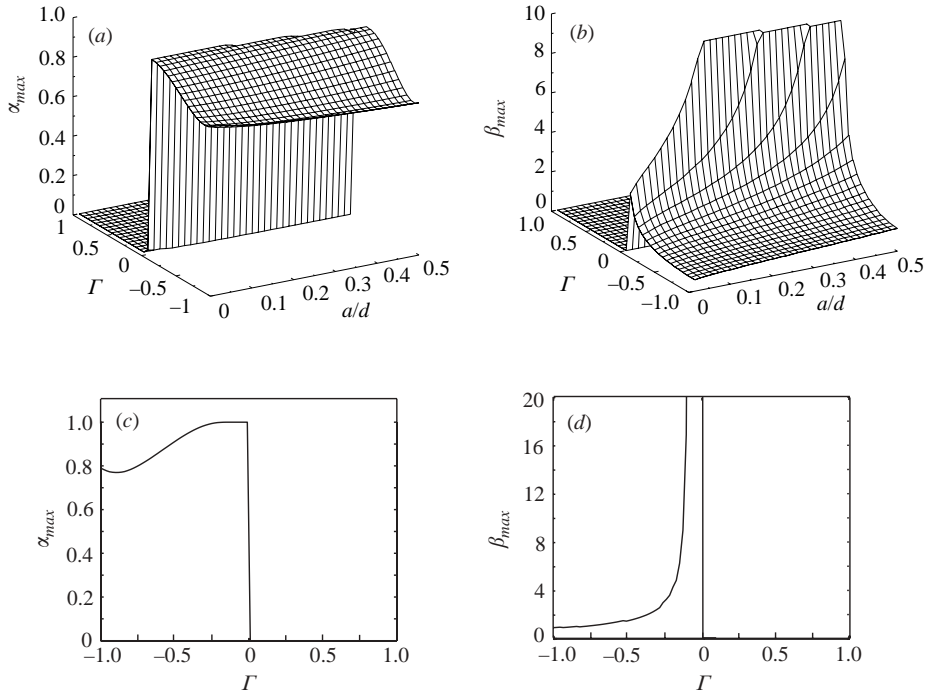


FIGURE 8. Maximum growth rate α_{max} (a) and corresponding wavenumber β_{max} (b) versus circulation ratio Γ and core size a/d for displacement perturbations for a vortex pair. (c), (d) Cross-sections at $a/d = 0.32$.

rises to a maximum value as $\Gamma \rightarrow 0$. The maximum growth rate has an upper value of 1.0: the perturbations can grow no faster than the strain rate $\tau = \Gamma_1 / (2\pi d^2)$ of vortex 1 on vortex 2. Co-rotating pairs ($\Gamma > 0$) are linearly stable to the long-wavelength perturbations (Jimenez 1975; Klein *et al.* 1995). As was argued in §2.2, the primary effect of changing the sign of Γ from negative to positive is to suppress instability for displacement modes. This also holds true in the coupled-perturbation analysis. Figure 8(c) shows a cut through the surface in figure 8(a) at $a/d = 0.312$, which corresponds to the cut-off distance to separation ratio of 0.2 used in Crow's paper. The value of $\alpha_{max} = 0.79$ at $\Gamma = -1$ is the growth rate for the Crow instability between two counter-rotating vortices. The maximum growth rate has a minimum value of 0.77 at $\Gamma = -0.89$ and exceeds the value for the Crow instability for $\Gamma \geq -0.77$. Figure 8(b) displays the surface of β_{max} . The most unstable wavenumber increases as Γ increases from -1 to 0. Consequently, the wavelength corresponding to the most unstable mode is smaller for dissimilar strength vortices. Figure 8(d) further illustrates this by plotting β_{max} vs. Γ at $a/d = 0.312$. It is also evident in figure 8(b) that at a fixed value of Γ , the most unstable wavenumber increases with increasing a/d , demonstrating that larger vortices are unstable to shorter-wavelength perturbations, particularly for small values of Γ .

3. Two symmetric vortex pairs: a four-vortex system

Four-vortex systems comprising two symmetric pairs have been used as models for analysing and exploring possible means of controlling the behaviour of the vortex

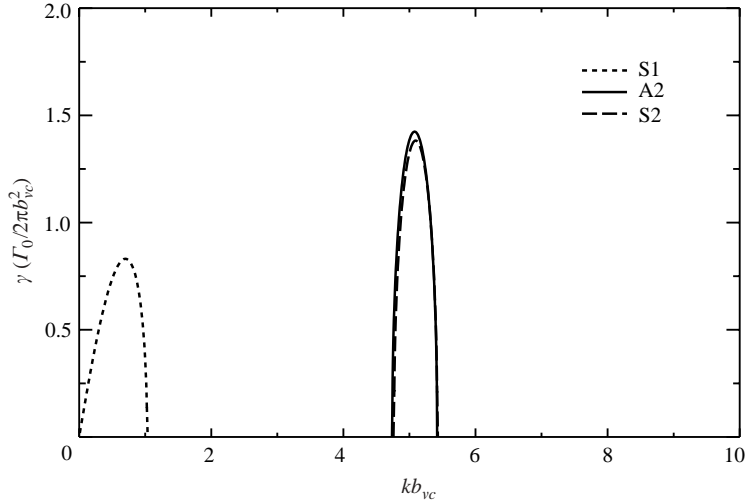


FIGURE 9. Growth rate curves for co-rotating vortex pairs: $\Gamma = 0.4$, $d/b_{vc} = 0.2$, $a/b_{vc} = 0.03$.

wake of large transport aircraft (Rossow 1999; Rennich & Lele 1999; Fabre & Jacquin 2000; Crouch, Miller & Spalart 2001; Ortega, Bristol & Savaş 2002; Fabre *et al.* 2002; Durston *et al.* 2004). The stability behaviour within a pair of vortices remains essentially unchanged when the separation of the vortices within the pair is much smaller than the separation between the two pairs. As the experimental vortices were produced in the wake of a lifting wing using a single in-board flap for the co-rotating vortex pairs and outboard flaps for the counter-rotating pairs, we now discuss the effect of the opposite vortex pair on the single-pair stability. Crouch (1997) presents the linear stability properties of two co-rotating vortex pairs, along with results mainly for $\Gamma = 0.5$. We present results from Crouch's governing equations for both the co- and counter-rotating pairs considered here. Additionally, we employ the Kelvin/Saffman rotation rate from equation (2.6) instead of the cut-off approximation, allowing the analysis to apply to the shorter-wavelength instabilities observed for the co-rotating case. The notation is the same as that of Crouch except when stated otherwise. We will use the vortex identification scheme employed by Crouch in his figure 1 and the method of classifying the instability modes from his figure 2: A1 and A2 for antisymmetric modes, and S1 and S2 for symmetric modes.

For the purposes of the present discussion, the essential result is that the effect of the symmetric opposite pair is minor compared to the instability within a pair when the pairs are far apart. The effects scale as the strain field, thus scaling as $(d/b_{vc})^2$, where d is the separation between the vortices within a pair and b_{vc} is the separation between the vorticity centroids of the pairs. Note that b_{vc} can be smaller or larger than b . As noted in Crouch (1997), the analysis strictly applies only in the case of vanishing $(d/b_{vc})^2$, although we believe that the trends observed here for finite $(d/b_{vc})^2$ are still valid.

3.1. Co-rotating vortex pairs

The growth rate curves for the case ($\Gamma = 0.4$, $d/b_{vc} = 0.2$, $a/b_{vc} = 0.03$), calculated using Floquet theory, are shown in figure 9. The S1 mode has a peak growth rate

of $\gamma = 0.82$ at $kb_{vc} = 0.70$. The S2 and A2 modes are unstable over a narrow band of wavenumbers and have almost identical growth rate curves. The reason for the close agreement between these growth rate curves is illustrated by considering the S2 and A2 eigenmodes at A2's most unstable wavenumber, $kb_{vc} = 5.07$. The eigenmodes of the right-hand-side pairs are almost identical, while those of the left-hand-side pairs are out of phase in the axial direction by π radians. As the vortex pairs are relatively widely spaced, the effects of this phase difference are minimal, such that the perturbation shapes on the left sides of the S2 and A2 modes become equivalent to one another. Note also that the relatively small growth rates (when scaled properly) are much less than those seen in §2 from the intra-pair instability involving the $n = 1$ self-rotation modes. Thus, for comparison to the experiments we will use only the results from §2 (to be discussed in parallel with CFD results in §4).

3.2. Counter-rotating vortex pairs

Figure 10 shows growth curves corresponding to some of the experimental data in Ortega *et al.* (2003). Figure 10(a) is for $\Gamma = -0.37$, $d/b_{vc} = 0.20$ and figure 10(b) for $\Gamma = -0.55$, $d/b_{vc} = 0.15$. The dashed curves are the growth rates of the two-vortex systems composed of flap and tip vortices. The vertical dotted and dashed-dotted lines are the experimentally measured instability wavenumbers on the port- and starboard-side flap vortices, respectively. The growth rate curves of the two- and four-vortex linear stability results are nearly the same. This is even more evident in figure 10(b), in which d/b_{vc} has a somewhat smaller value of 0.15. The experimentally measured wavenumbers all lie within the range of unstable wavenumbers. The port-side flap vortex consistently exhibits a higher-wavenumber instability than that on the starboard-side vortex, which may be due to an asymmetry in the strut or airfoil construction (see Ortega *et al.* 2003). For the majority of the runs, the differences between the linear stability results of the single-vortex pairs and those of the two-vortex pairs are small, indicating that the instability is caused by the interactions of the flap and tip vortices within each of the counter-rotating pairs. The experimental wavelengths are on the order of the separation distance of the pairs or about four times the separation distance of the vortices within a pair. This wavelength is shorter than that of the classical $\Gamma = -1$ Crow instability, which predicts a most unstable wavelength of order 8–10 times the separation distance. These observations are consistent with §2.3 which shows that for fixed a/d , the most unstable wavelength decreases as $\Gamma \rightarrow 0^-$.

The calculations of Fabre *et al.* (2002) for an optimal growth rate of instabilities for a vortex system corresponding to that seen in figure 2(c) demonstrate remarkable corroboration of the results in figure 10(a). They find that for $\Gamma = -0.37$, the optimum growth, as defined in their equation (3.1), occurs at a wavenumber of $kb_{vc} \approx 7$ which agrees well with that in figure 10(a). The corresponding optimal growth rate is the highest value marked in their figure 2 for periodic configurations!

One possible reason for the difference between the theoretical and experimental wavelengths is that the self-induced rotation rate does not account for axial flow in the vortex core. During several preliminary experiments, air bubbles were injected into the vortex cores. The air bubbles, which became trapped in the vortex cores, were observed to travel in the same direction as the airfoil, indicating the presence of axial flow. Others (Ciffone & Orloff 1974; Devenport, Vogel & Zsoldos 1970) have also shown the existence of axial flow in vortex cores. For the present set of experiments, no axial flow measurements were made in the vortices, making it difficult to quantify the axial flow in the vortex cores. Lastly, the helix angle between

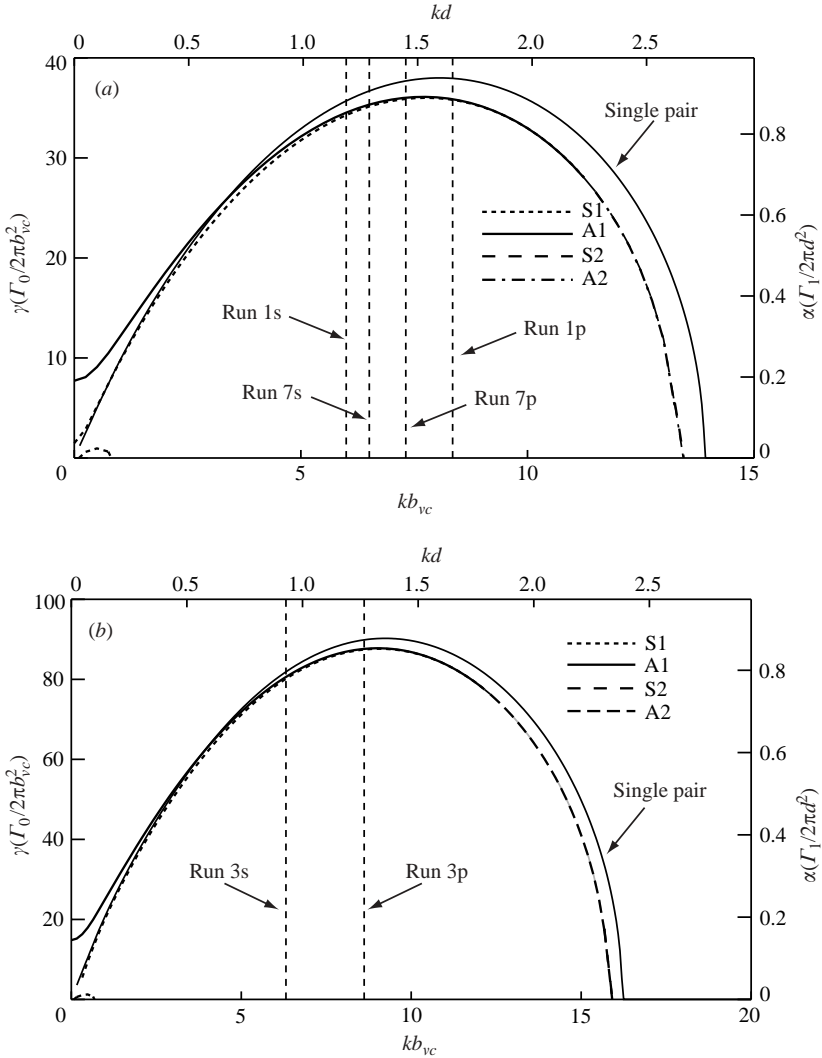


FIGURE 10. Comparison of observations with the predictions of two- and four-vortex linear stability analyses. (γ, kb_{vc}) axes are for two vortex-pair systems and (α, kd) axes are for both an isolated vortex pair and individual pairs within the two vortex-pair systems. The plots are based upon the average core sizes, relative circulation strengths, and initial separation distances from PIV measurements. Run numbers refer to flow visualization experiments in table 3 of Ortega *et al.* (2003). The vertical lines indicate the observed instability wavenumbers on the port-side, p, and starboard-side, s, flap vortices from flow visualization. (a) $\Gamma = -0.37$, $d/b_{vc} = 0.20$ and (b) $\Gamma = -0.55$, $d/b_{vc} = 0.15$.

the vortices, however small, may introduce slight differences between the experimental and theoretical wavelengths.

4. Numerical simulations

A numerical investigation was carried out to remove the restrictions inherent in the linear analysis and follow the eventual nonlinear fate of the linear instability

modes for comparison with the experiments. Further, the numerical results provide complete knowledge of the velocity $\mathbf{u} = (u, v, w)$ and vorticity $\boldsymbol{\omega} = (\omega_x, \omega_y, \omega_z)$ fields as functions of space and time, showing a detailed and three-dimensional development of the flow not accessible from the experiments.

The computational fluid dynamics (CFD) code employed is a spectral Navier–Stokes initial-value code in cylindrical coordinates, developed by Matsushima & Marcus (1997). The basis functions are periodic in the azimuthal and axial directions. An algebraically mapped set of rational Legendre functions is used in the radial direction. The code satisfies the pole condition exactly and avoids stiffness problems there. A simple ∇^4 hyperviscosity is used to suppress the buildup of energy at small length scales, effectively acting as a large-eddy simulation (LES) model for turbulence. Further details may be found in Matsushima (1995), Matsushima & Marcus (1995) and Matsushima & Marcus (1997). In all simulations, vortices are initialized as Gaussian vortices of size $\sigma = 1$ cm. The strength of the stronger vortex is fixed as $\Gamma_1 = 2\pi \text{ cm}^2 \text{ s}^{-1}$. The Reynolds number is, thus, varied by changing the kinematic viscosity. All results shown are checked to hold under variations in the time step, the number of modes, the length of the computational box, and the amplitude of the initial perturbation. For the linear growth-rate results, the effects of turbulence are not important, as the early phases of the flow are laminar. At later times, turbulence does arise; however, we focus only on the gross features of the flow and not the turbulent details.

4.1. Counter-rotating wavelength of maximum growth

Growth rates from the CFD code for Gaussian counter-rotating vortex pairs corresponding to experimental conditions were compared to those predicted by the linear theory. We began each run at $t=0$ with a perturbation on each vortex, with relative amplitudes given by the eigenvector for maximum growth rate from the vortex filament analysis. For the case $\Gamma = -0.37$, $d/\sigma_1 = 3.96$, $d/\sigma_2 = 7.47$, this procedure yields a wavenumber of maximum growth of $k\sigma = 1.6 \pm 0.05$, with the uncertainty based on the finite number of modes used in the axial direction, which is in agreement with the most unstable wavenumber for a single pair of $(k\sigma)_{\max} = 1.594$. The growth rates also compare well, with $\alpha = 0.89$ from CFD, and $\alpha = 0.94$ from the linear theory. Thus, even though d/σ is outside the presumed range of its applicability, the linear stability analysis remains useful.

4.2. Co-rotating wavelength of maximum growth

The linear stability theory predicts that co-rotating vortex pairs are unstable to elliptic perturbations. The importance of such modes for a finite vortex is studied by perturbing a single vortex in a strain field only (no rotation) with noise at $t=0$ and then observing which mode appears first. The strength of the externally imposed strain field was 0.0225, which is that found at a distance of $d = 6.67\sigma$ from a vortex of strength $2\pi \text{ cm}^2 \text{ s}^{-1}$. A dominant mode appears with a wavenumber of $k\sigma = 2.28 \pm 0.04$, with the uncertainty resulting from the finite number of modes (256) used in the axial direction. A cross-section of the vortex shows the core to be noticeably displaced to one side, consistent with the $n=1$ elliptic instability. These results are in agreement with those of Eloy & Le Dizès (1999), who found an elliptically perturbed Gaussian vortex in a weak strain field to grow most quickly at an axial wavenumber of $k\sigma = 2.26$.

This result can be further checked by computing the growth rate for single perturbations at different wavenumbers. In this procedure, a small-amplitude (0.001σ)

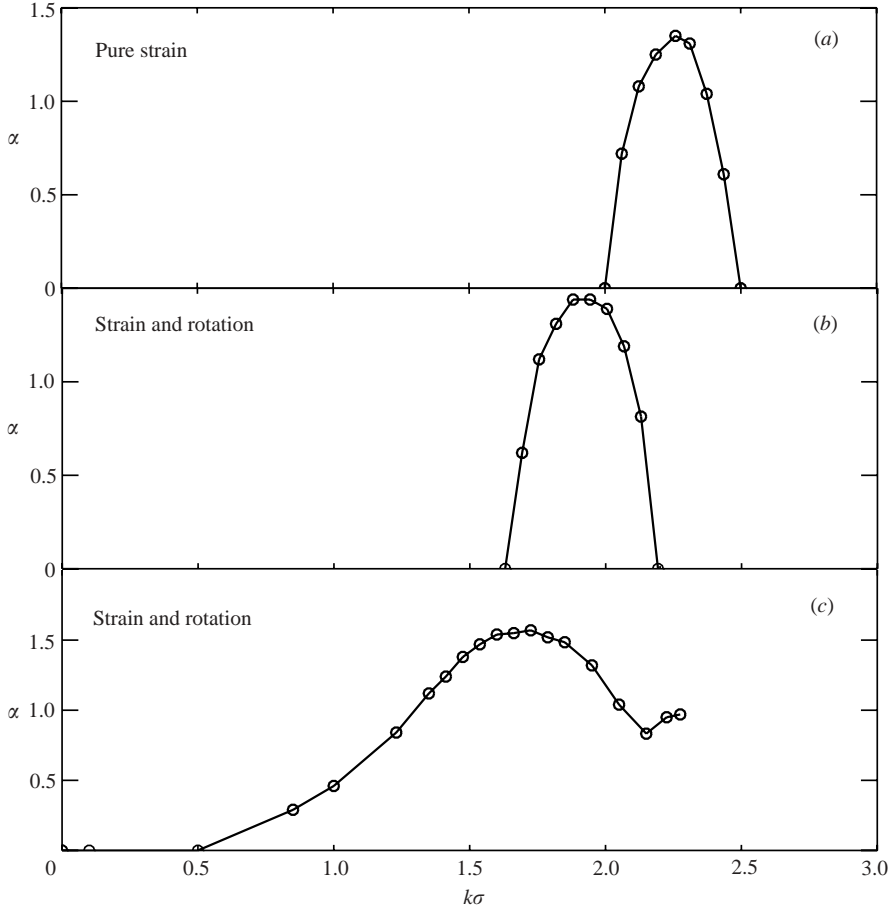


FIGURE 11. Growth rate vs. wavenumber for a Gaussian vortex embedded in (a) a weak strain field only; (b) a strain and rotation field for $(\Gamma, d/\sigma) = (0.9, 6.67)$; (c) a strain and rotation for $(\Gamma, d/\sigma) = (1.0, 5.0)$.

displacement mode is excited at a given wavenumber at $t = 0$. After a short time, this (stable) displacement mode makes a transition to the (unstable) elliptic mode and then grows exponentially, demonstrating the coupling between them. Figure 11(a) shows the results of this procedure for a vortex in a weak strain field without rotation. The peak growth rate is 1.35 and occurs at a wavenumber of about 2.25. This is close to the values of 1.38 and 2.26, respectively, from Eloy & Le Dizès (1999). Note that these values are higher than the growth rates given by the linear theory, which is due to the fact that the elliptic mode creates additional internal strain not accounted for in §2.

The experimental flows for the co-rotating cases are simulated by applying this procedure to a single vortex, embedded in external strain and rotation fields calculated from a point-vortex analysis, and with the experimentally determined strength and separation values. For the $d/\sigma = 6.67$ case, the appropriate strain and rotation rates are 0.0225 and -0.0428 . For $d/\sigma = 5.0$, they are 0.04 and -0.08 . The resulting growth curves are shown in figure 11(b, c). While the growth rate curve for the $d/\sigma = 6.67$ case is narrow with a sharp peak at a specific wavenumber (figure 11b), the curve

Γ (Γ_2/Γ_1)	d/σ_1	d/σ_2	$(kd)_{max}$ linear theory	$(kd)_{max}$ CFD	$(kd)_{max}$ experiment	
-0.37	3.96	7.47	1.6	1.6	1.4 ± 0.3	Ortega (2001)
0.90	6.67	6.67	13 (11)	13	6.7 ± 2	Bristol (2000)
1.00	5.00	5.00	8.5 (7)	8	6.5 ± 2	Bristol (2000)

TABLE 1. Most unstable wavenumbers for a vortex pair. Γ is circulation ratio, d vortex separation, σ Gaussian vortex core size. Wavenumbers are from the linear theory of §2, CFD results of §4, and experimental results from Bristol (2000) and Ortega (2001). Theoretical numbers in parentheses are values obtained by using a value of d taken at the vortex half-orbit location, rather than the geometrical tip-to-flap distance.

for the $d/\sigma = 5.0$ case (figure 11c) is noticeably broadened. This still implies that a single wavelength should emerge from noise, but the width of this curve suggests that a broader range of wavenumbers may be actually observed in experiments. The breadth of this curve may be due to the large change in cross-section experienced by the vortex in this case.

Eloy & Le Dizes (1999) also found that a Gaussian vortex in a strain field has additional unstable modes with more than one radial node. In particular, a Gaussian vortex has an $n=2$ mode, with a peak at $k\sigma = 3.95$. This mode may have been shifted by the orbit-induced rotation and broadened enough by straining effects to show up as a rise at the high-wavenumber end of the curve in figure 11(c). These higher-wavenumber modes, however, are less likely to show in a real flow, due to the increased effects of viscosity and, possibly, a more limited capacity for growth to large amplitudes.

In the results above, the presence of a second vortex is simulated only by an imposed strain field and solid-body rotation. Simulations with an actual vortex pair produce essentially the same curve for the more widely spaced pair, but with some difference for the more closely spaced pair. For $d/\sigma = 6.67$, $(k\sigma)_{max}$ is still 1.7. For the $d/\sigma = 5.0$ case, $(k\sigma)_{max}$ is shifted to a slightly lower value, 1.6, and occurs at a higher growth rate, 2.0. This larger growth rate may be the result of two-dimensional and three-dimensional instabilities becoming somewhat entangled. Also note that these vortices are near the critical separation distance for merger in two dimensions, meaning that at places where the vortices are brought closer together accelerated two-dimensional growth may be experienced (Bristol 2000; Matsushima 1995).

4.3. Most-unstable wavelength: theory, CFD, and experimental comparison

The results are summarized in table 1. For the case of $\Gamma = -0.37$ and 1.0, the simulations predict wavenumbers within experimental uncertainty. But for the case of $\Gamma = 0.9$, the prediction is a factor of 2 too high. There are a number of issues which may explain this discrepancy, in particular experimental uncertainties in the vortex parameters used as input into the computations. The value of σ is determined by fitting a Gaussian to an azimuthally averaged vorticity distribution. This, and the finite size of the PIV interrogation windows, results in some uncertainty in σ . This can have a significant impact on the wavelength predictions: for example, increasing σ by 25% for the case $d/\sigma = 6.67$, yields the value given for the $d/\sigma = 5.0$ case, thus changing $(kd)_{max}$ from 13 to 8.5. The vortices do not exist at $t=0$ as perfectly parallel

entities, but are formed from a wing. This most directly affects the separation distance d , which changes somewhat as the wake rolls up into the vortex pair. The experimental values for d for the co-rotating case were simply taken as the geometrical separation between the tip and flap edges of the wing used in the experiments in table 1. Using, instead, the separation near the half-orbit point changes the values of kd from 13 and 8.5 to 11 and 7, respectively, improving the agreement between theory and experiment. The counter-rotating vortex separation distances are better determined, as they only fluctuated slightly before the instabilities become significant. These uncertainties could be responsible for much, but probably not all, of the differences in table 1.

Two aspects not captured by either the simulations or theory are the helical path of the vortices and the upstream–downstream asymmetries of the flow in experiment. The experimental wakes are created as the wing travels through the fluid, thus producing a helical path as the pairs orbit. This helix pitch decreases for the co-rotating vortices as they spiral inwards towards merger (figure 1 of Bristol *et al.* 2003). At a given location, this means that the flow upstream involves more widely separated vortices than the flow downstream. Another significant difference between the predictions for counter- and co-rotating instabilities is that the latter requires the internal elliptic mode, whose dispersion relation is likely to be more sensitive to internal vortex structure and, thus, to experimental uncertainties in σ .

Numerous observations suggest that axial flow may also be present in the vortices, particularly at early times (Ciffone & Orloff 1974; Devenport *et al.* 1970). As shown in the asymptotic formula by Moore & Saffman (1975), the axial flow has the effect of shifting the peak in the growth curve for the counter-rotating case. For example with a peak axial velocity of 0.25 (compared to the peak azimuthal velocity of 0.638), helical modes appear in the vortex (Bristol 2000). This suggests that the resonance between modes $\exp(im\theta)$ and $\exp(-im\theta)$, which previously summed to give a planar wave, has been broken. Even stronger levels of axial flow can destabilize the vortex even without a strain field (Lessen, Singh & Paillet 1974). As no obvious helical modes were observed in the experiments, we presume that the axial flow rates must be small. Since we do not have axial flow data for these vortices, we do not attempt to include this effect in the predicted value of $(k\sigma)_{max}$.

Overall, though, the results of table 1 are remarkable considering the simplicity of the model compared to the experimental wake-vortex flows. The two are also in agreement in form, as the instability in both cases is sinuous, planar, and grows in near alignment with the extensional axis of the strain field (Bristol *et al.* 2003; Ortega *et al.* 2003).

4.4. *Eventual fate of the elliptic and displacement instabilities*

Experimentally, the co-rotating vortices merge, while the counter-rotating vortices produce rings (figure 2). Can the linear modes of instability lead to these results? To answer this question, we allow the CFD code to run beyond the point of early growth and observe the eventual nonlinear fate of the instabilities.

4.4.1. *Co-rotating case*

Figure 12 shows surfaces of vorticity for a co-rotating vortex pair for $(\Gamma, d/\sigma) = (0.9, 5.45)$, taken as a representative example of the experimental cases. At $t = 0$, the weaker vortex is perturbed with the wavenumber of maximum growth ($(k\sigma)_{max} = 1.8$ for this case), at an amplitude of 0.001σ . Molecular viscosity ν is used in this run, with $Re_\Gamma = (\Gamma_1 + \Gamma_2)/\nu = 10^5$, which is of the same order as that in the experiments.

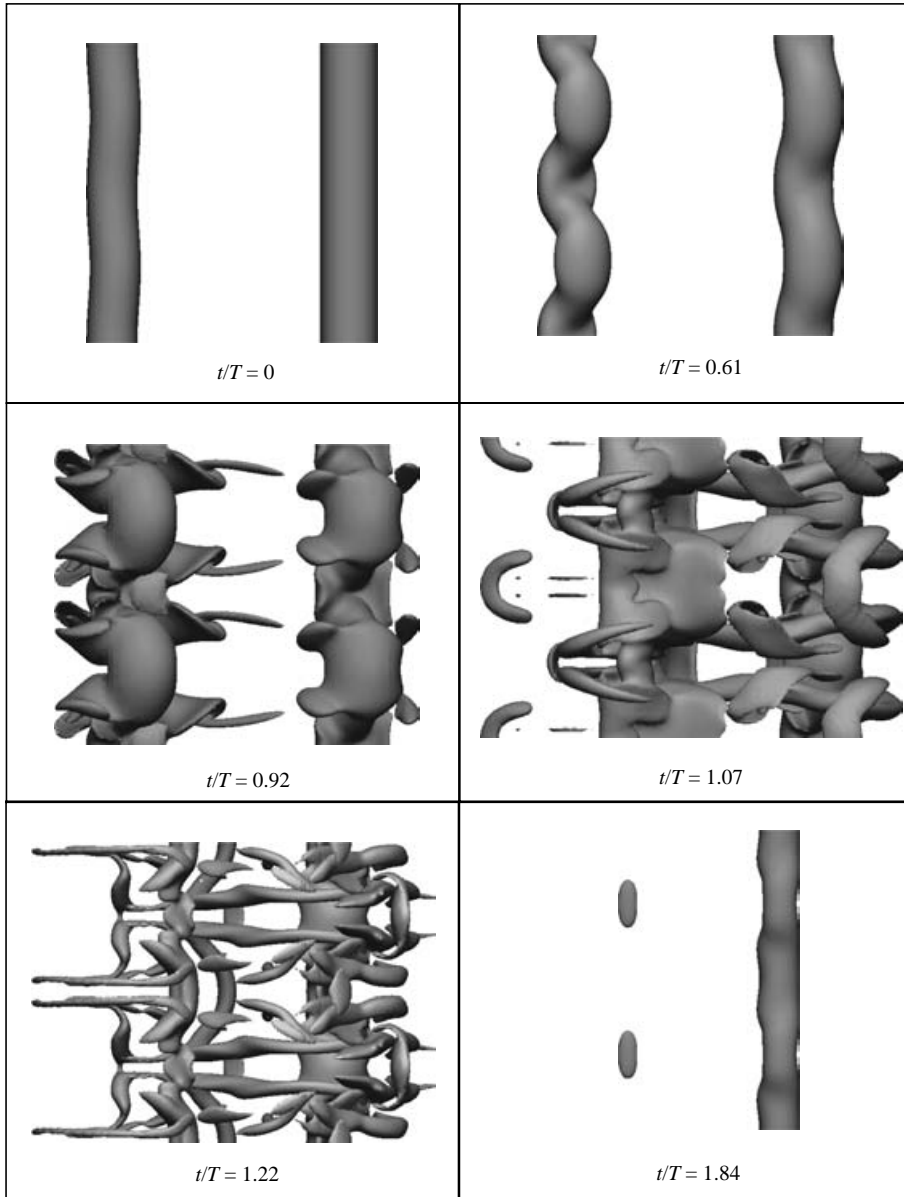


FIGURE 12. Simulation of the co-rotating case $(\Gamma, d/\sigma) = (0.9, 5.45)$. Flap vortex was perturbed at $t = 0$ with a wavenumber $k\sigma_{max}$. Surface taken at $|\omega| = 1.35 \text{ s}^{-1}$, corresponding to $r = 0.63\sigma$ on stronger vortex. Frame $t/T = 0.61$ corresponds to figure 13. Orbital period $T = 98 \text{ s}$.

128 modes were used in the radial direction, 256 in the azimuthal, and 64 in the axial direction. The domain is one wavelength long; the results show two wavelengths. The surface of vorticity shown corresponds to that at $r = 0.63\sigma$ on the stronger vortex, or equivalently at 0.54σ on the weaker one. The view is maintained approximately perpendicular to the vortex pair. The orbital period T for a point-vortex pair at these conditions is 98 s. At time step $t/T = 0.62$, an elliptic instability has grown to

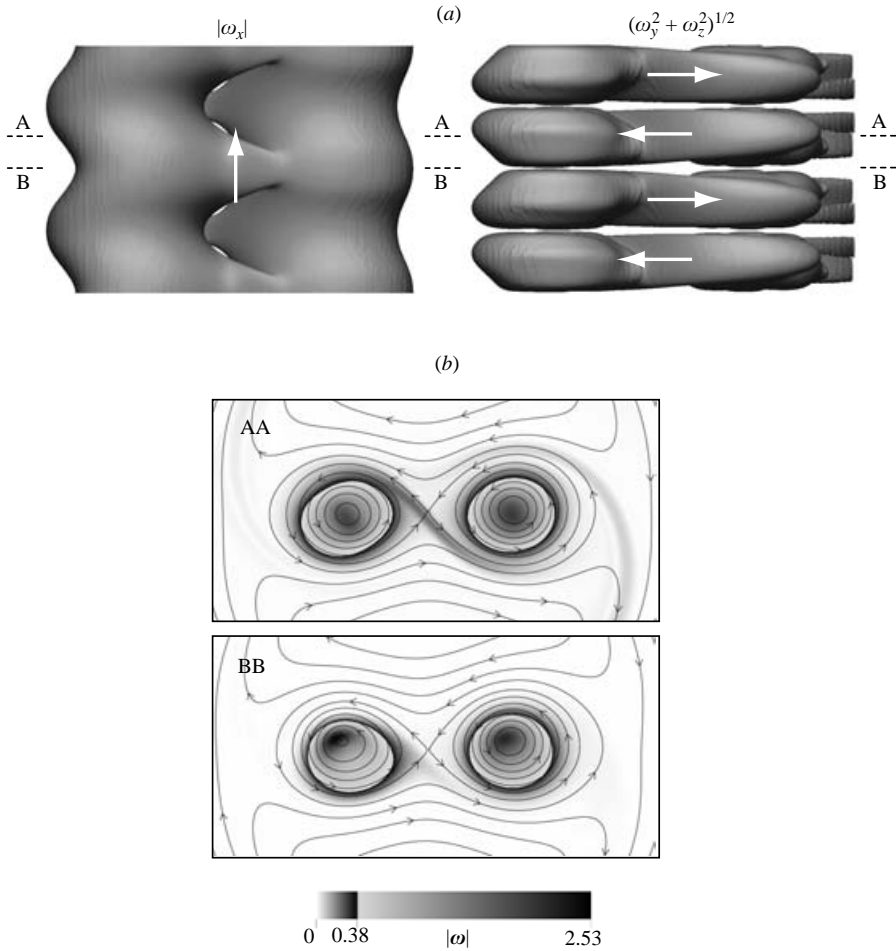


FIGURE 13. (a) Surfaces of axial vorticity magnitude $|\omega_x|$ and cross-plane vorticity magnitude $(\omega_y^2 + \omega_z^2)^{1/2}$ from the co-rotating pair in figure 12 at $t/T = 0.61$. Surfaces are taken at a level of $|\omega| = 0.03 \text{ s}^{-1}$, which corresponds to a distance of 2.05σ on the stronger vortex. The arrows indicate the senses of the respective vorticity components. (b) Cross-plane streamlines in the rotating reference frame of the pair, overlaid on vorticity magnitude $|\omega|$ at cross-sections AA and BB shown in (a). The grey-scale bar used in (b) is double-valued to highlight the small values of vorticity outside the vortex cores.

a large amplitude on the weaker vortex, and has also become noticeable on the stronger vortex. Both are aligned approximately along the respective strain fields. By $t/T = 0.92$, thin bridges of vorticity extend from the weaker vortex to the stronger, which begin to link the two. As time progresses, these bridges grow in a complex manner, finally bringing the two into merger.

Figure 13 indicates an early stage in the formation of the vorticity bridges. Shown in figure 13(a) are surfaces of axial vorticity $|\omega_x|$ and cross-plane vorticity $(\omega_y^2 + \omega_z^2)^{1/2}$ at a relatively low level of vorticity magnitude $|\omega|$, corresponding to a location of $r = 2.05\sigma$ on the stronger vortex. The arrows drawn on the surfaces indicate the general direction of vorticity on the bridges. Figure 13(b) shows the streamlines taken at two different

cross-sections. The grey scale on the streamlines corresponds to the magnitude of total vorticity. The grey-scale bar used in (b) is double-valued to highlight the small values of vorticity. The origin of the bridges of vorticity is suggested in horizontal streamlines in the rotating reference frame of the pair, taken at the cross-sections AA and BB and displayed in figure 13(b). In section AA, corresponding to a slice in the bridge of vertical vorticity, the periphery of the vortex has been forced outside the bounding streamlines, as expected with the elliptic instability. This peripheral vertical vorticity is advected over to the partner vortex, creating the bridge of vorticity seen in the $|\omega_x|$ surface.

The edges of this bridge are then turned and stretched against the stagnation streamlines, as can be seen in section BB. These stretched edges become apparent as the bridges in the horizontal surface. In later stages of the flow, these bridges strengthen, eventually leading to merger of the two, as seen in figure 12.

4.4.2. Co-rotating case – single hump

One could argue that any disturbance which is large enough to bring the two vortices together might initiate merger, and that the elliptic mode is only necessary for infinitesimal perturbations. A simple way of partially addressing this question is presented in figure 14, in which one vortex filament has been displaced by a finite Gaussian hump of amplitude 2σ for a $d/\sigma = 6.67$, $\Gamma = 0.9$ pair (figure 14). Such a hump can be viewed as being formed by an infinite range of finite perturbations, thus serving as one way to see whether modes other than those considered in the linear instability analysis might also lead to merger. After a short period of time, the initial hump transitions into a higher-frequency set of modes, which have approximately the same wavelength as those for the elliptic instability, and bear some structural resemblance to it (compare $t/T = 0.68$ in figure 14 with $t/T = 0.61$ in figure 13). A run with a weaker hump of amplitude σ (not shown) in fact makes a clear transition to the elliptic instability. Humps with an amplitude of more than 2σ merge in a more complicated fashion without the clear appearance of any particular modes. Although not the final word on the subject, this suggests the elliptic instability to be a relatively robust precursor to merger.

4.4.3. Counter-rotating case: single-vortex pair

Figure 15 shows the results of a run for $\Gamma = -0.37$, $d/\sigma_1 = 3.96$ and $d/\sigma_2 = 7.47$. The weaker vortex is perturbed at the most unstable wavelength at $t = 0$. The values of Re_Γ and hyperviscosity are the same as those used in figure 12. The viewpoint is such that at $t = 0$ the weaker vortex is in the foreground, and then begins its orbit around the stronger vortex. At $t/T = 0.38$, the displacement perturbation has grown, and has brought the peaks of the perturbation closer to the dominant vortex. The sections of the weaker vortex in close proximity experience a larger induced velocity field, causing them to wrap around the stronger vortex, similar to the calculations of Klein *et al.* (1995), Quackenbush *et al.* (1997), and Marshall *et al.* (2001). The sections farther from the strong vortex are pushed out, forming the loops at $t/T \approx 0.74$. As the wrapping continues, the ends of the loop are brought together, and the loop itself begins to self-induce away from the dominant vortex. Eventually, the loop pinches off to form a vortex ring.

4.4.4. Counter-rotating case: two symmetric vortex pairs

Simulations of the four-vortex wake provide a remarkable description of how the loop/ring ejected from one counter-rotating pair can affect the opposite vortex pair.

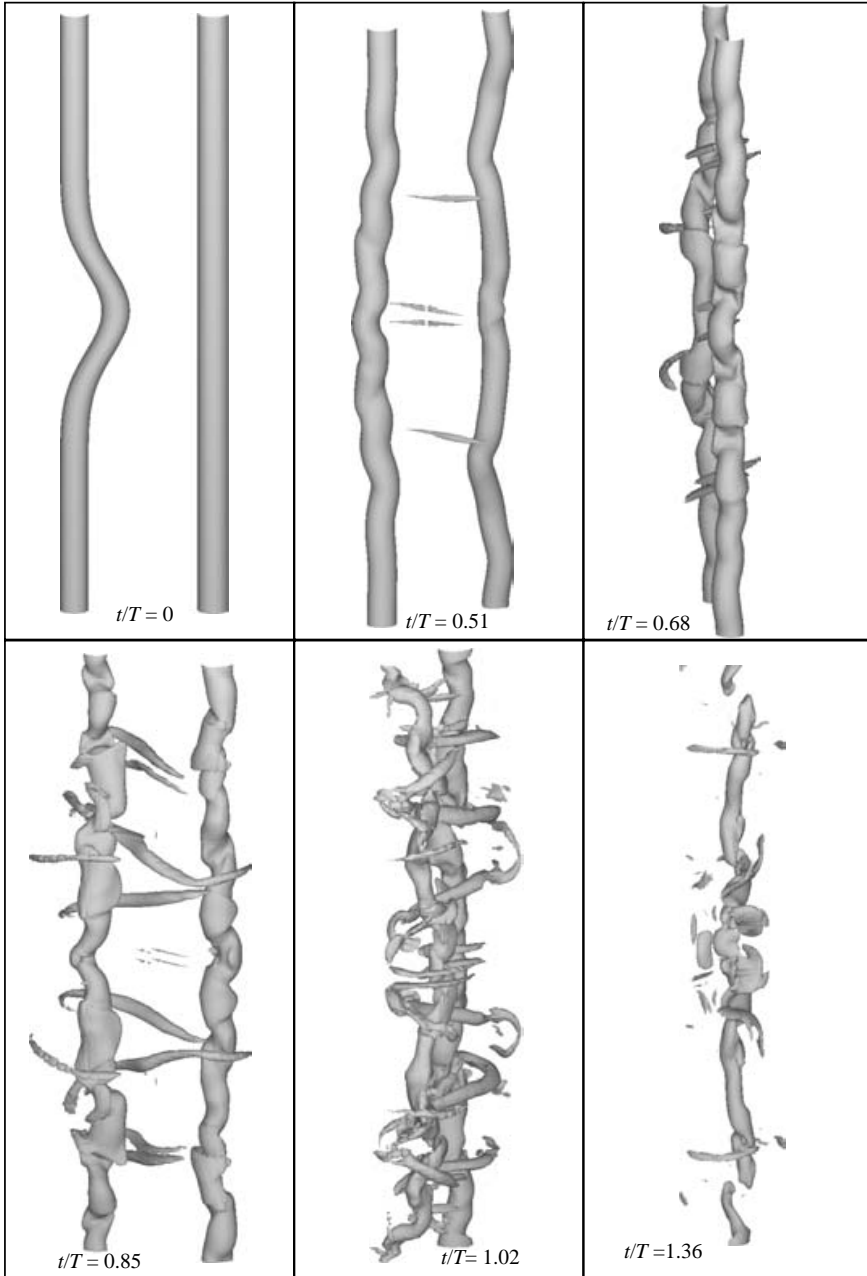


FIGURE 14. Simulation of a $(\Gamma, d/\sigma) = (0.9, 6.67)$ co-rotating pair perturbed by a hump of amplitude 2σ on the weaker vortex. Some indication of elliptic instability is visible at $t/T = 0.68$ (compare to $t/T = 0.61$ in figure 12). Vorticity bridges become clearly visible at $t/T = 0.85$. Orbital period $T = 147$ s.

Figure 16 shows the result of a run for two pairs of vortices like that in figure 15 initially placed at $b_{vc}/d = 5.46$. The outboard vortices were perturbed 90° out of phase. This run used 128 modes in the radial, 256 in the azimuthal, and 64 in the axial directions, such that about 10 collocation points span a given vortex core.

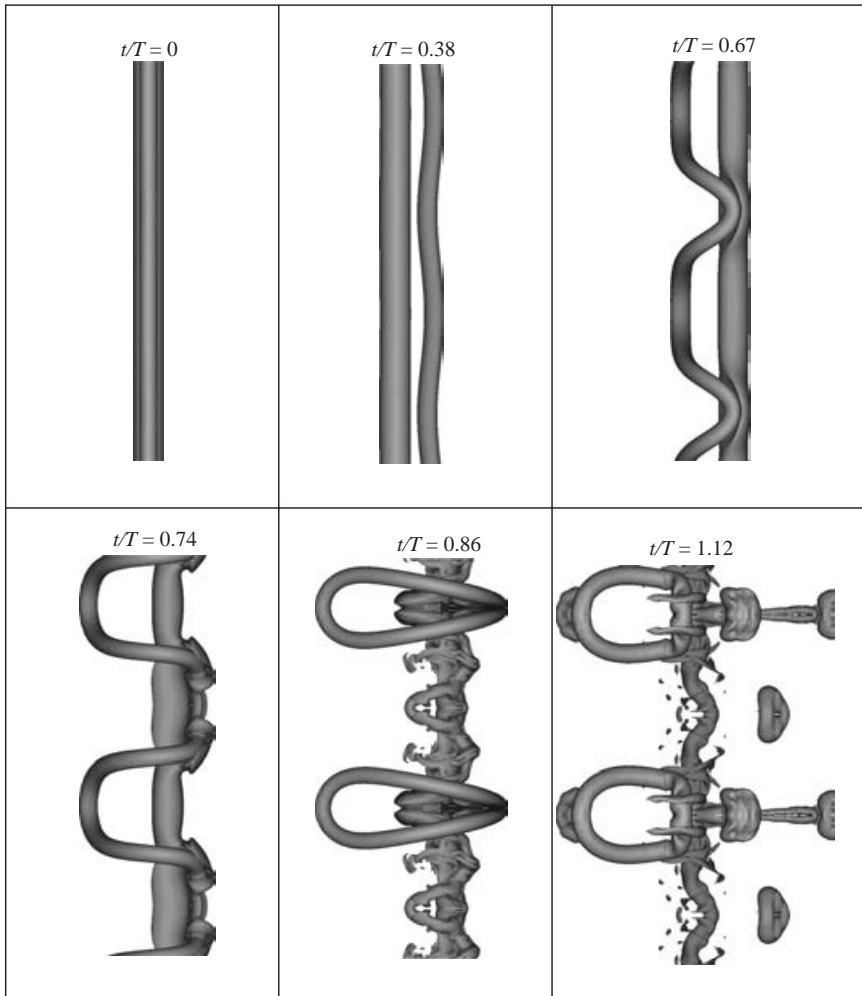


FIGURE 15. Surfaces of a $\Gamma = -0.37$, $d/\sigma_1 = 3.96$, $d/\sigma_2 = 7.47$ counter-rotating pair. The weaker vortex is perturbed at $(kd)_{max}$ at $t = 0$. View is edge-on at $t = 0$, with the weaker vortex in the foreground, and remains fixed throughout the simulation. Orbital period $T = 156$ s.

$Re_\Gamma \approx 63\,000$, although the coefficient of hyperviscosity is as large as that of molecular viscosity for this case. The relatively high level of vorticity chosen for the surface of figure 16 ($|\omega| = 1.35\text{ s}^{-1}$) appears to nearly disappear at large times ($t/T > 1.2$). Surfaces at much lower levels of vorticity (not shown here) show that there is still a wake, but that it has lost some of its coherence and much of its concentration. Similar behaviour can be seen in the PIV data of Ortega *et al.* (2003). The behaviour seen in figure 16 bears a remarkable resemblance to the experimental data (figure 2c) and Ortega (2001), where this behaviour was first observed. Flow visualizations show the formation of the vortex rings, which cross over to the other side of the wake and interact strongly with the other vortex pair (figure 2c). PIV data (see Ortega 2001 and Ortega *et al.* 2003) show the loss of coherence of the wake at later times. Independently, Fabre *et al.* (2002)'s linear analysis of four-vortex systems for

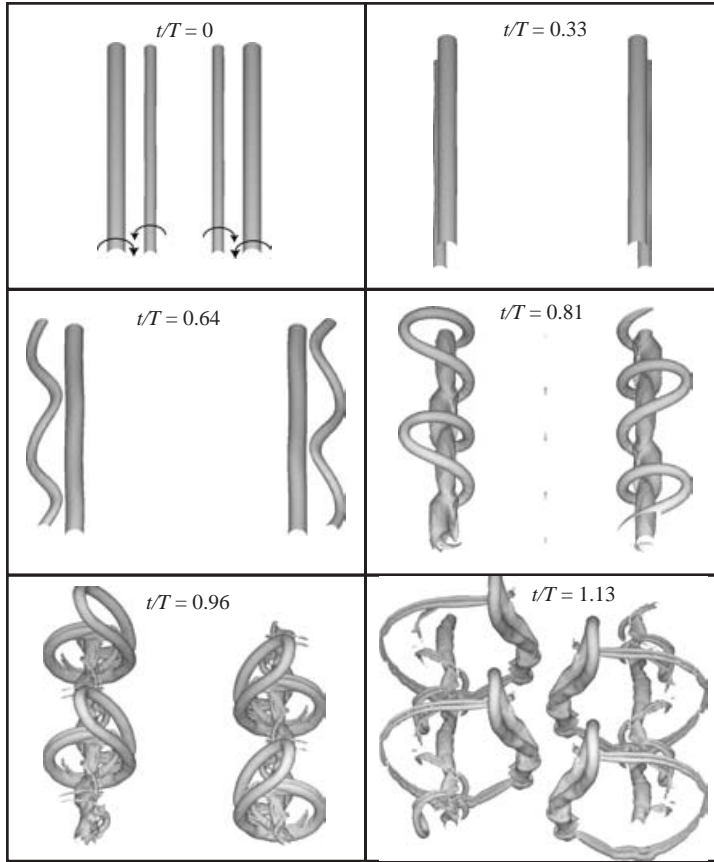


FIGURE 16. Isovorticity surfaces of two counter-rotating vortex pairs. Each pair has the same properties as that in figure 15, except that one pair has the senses of circulation reversed to establish symmetry. $\Gamma = -0.37$, $b_{vc}/d = 5.46$. Orbital period $T = 156$ s.

optimal growth confirms the remarkable initial growth rate of the instabilities for a configuration very close to that in figure 16.

4.5. Experimental evidence for vorticity bridges

Visual evidence for the presence of the vorticity bridges (§4.4.1) is shown in figure 17. The evidence in these figures was noticed in a few cases after the data of Bristol (2000) were revisited following the suggestions of the numerical calculations presented in figure 13. The dye was introduced at the cores of the vortices, and, hence, initially marks the highest level of vorticity. Since the Reynolds number is moderately high, diffusion is not expected to be a significant factor, and therefore, the vorticity at the perimeter of the vortex will be only faintly marked by the dye. The vorticity bridges that are forming at the fringes of the vortex are, at best, weakly marked by the dye, hence the faint images. Since the vorticity bridges occur at very low levels of vorticity, the grey scale of the images is stretched at the lower end to bring out these details. The round halos at the centres of the images result from this stretching. The circulation ratio is estimated from PIV data as $\Gamma \approx 0.8$. The dye bridges become visible after about 3/4 orbit of the pair of vortices generated from the tip and flap

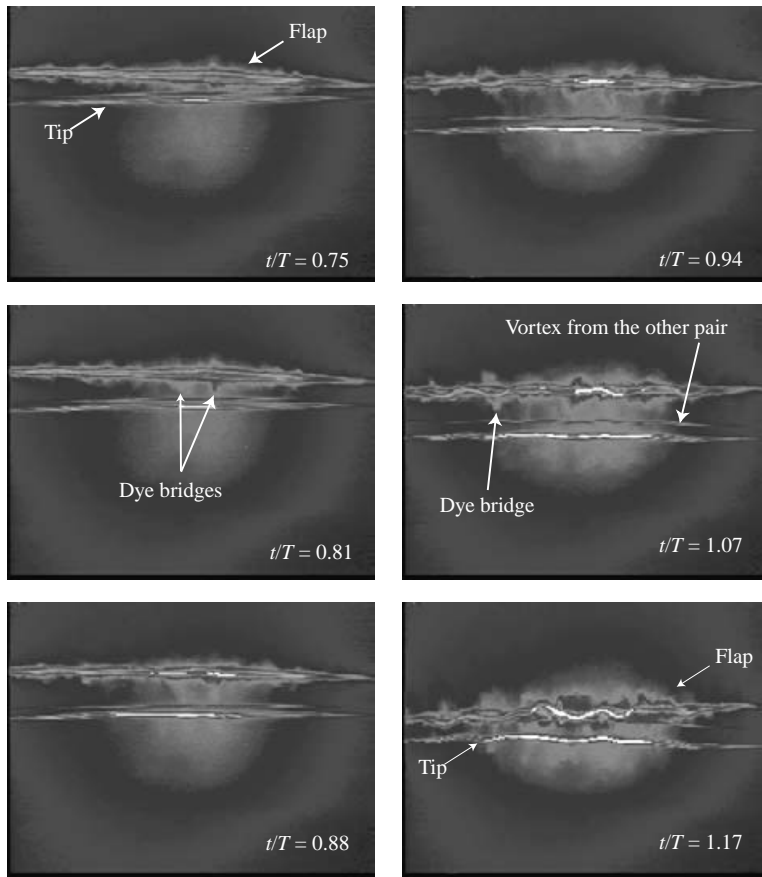


FIGURE 17. Side-view flow visualization photos showing the dye bridges between a co-rotating vortex pair before merger. $U = 500 \text{ cm s}^{-1}$, $b = 40 \text{ cm}$, $d/b_{vc} \approx 0.4$, $\Gamma \approx 0.8$, $T \approx 2.50 \text{ s}$. The wing is traveling from left to right.

of the wing. As the pair continues orbiting, the dye bridges start wrapping around the stronger tip vortex as the CFD results in figure 13 predicted. At later times, the elliptical mode of instability on the weaker flap vortex becomes evident in the last two frames in the figure as the core and periphery go in opposite directions. There is also some indication of concurrent elliptical instability on the stronger tip vortex.

Figure 18 shows axial vorticity contours of an experimental co-rotating vortex pair taken from PIV data. Similar to figure 17, the scale is stretched so that very low levels of vorticity can be visualized at the expense of clarity of high vorticity levels in vortex cores. Since the waves are nearly stationary in the laboratory reference system, the PIV measurement plane is also fixed with respect to the instability wave and vorticity bridges. The stronger tip vortex is in view at $Ut/b = 41$, as well as part of a vortical band between the two. The weaker vortex enters the view at $Ut/b = 48$, where the vorticity bridge is now clearly visible. The bridge wraps around the stronger vortex during the merger, as seen in the later frames in the figure.

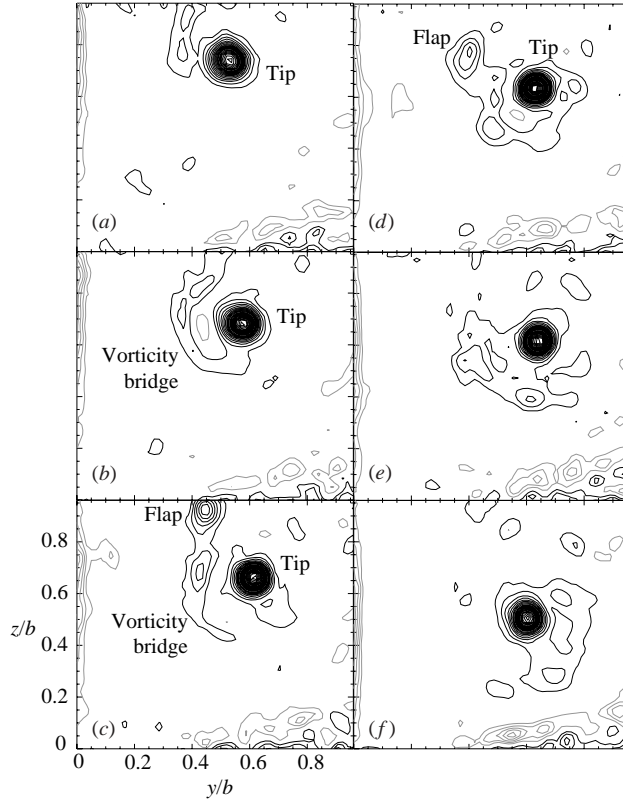


FIGURE 18. Experimental vorticity contours showing evidence of vorticity bridges. $U = 200 \text{ cm s}^{-1}$, $b = 40 \text{ cm}$, $T \approx 5.6 \text{ s}$, $d/b_{vc} \approx 0.4$. Contour increment is kept small to highlight the vorticity bridge, hence the high contour density at the vortex core. (a) $Ut/b = 41$, (b) 45, (c) 48, (d) 52, (e) 55, (f) 62.

5. Summary

Results from linear stability analyses and CFD calculations are presented to provide explanations for recent experimental observations of instabilities between unequal wake-vortex pairs. Experimentally, co-rotating pairs were observed to merge after the appearance of a short-wavelength sinuous disturbance. For counter-rotating pairs, a relatively long-wavelength disturbance was observed to grow on the weaker vortex, evolving into large loops and then rings extending out from the pair.

Extending the linear stability analyses of Crow (1970) and Widnall *et al.* (1974) by accounting for the orbital motion of an unequal pair illustrates the mechanism behind these instabilities. As before, rotation of planar perturbations must be overcome for the strain field to cause instability. This requires that self- and orbit-induced rotation partially cancel, which requires self-induction to act in a retrograde sense for a counter-rotating pair and in a prograde sense for a co-rotating pair. This in turn allows counter-rotating pairs to be destabilized by long-wavelength displacement perturbations, whereas co-rotating pairs may be destabilized by shorter-wavelength elliptic perturbations.

Using the linear technique of Crouch (1997), the effects of an additional symmetric pair are seen to be minor for separations only moderately larger than the intra-pair

distance. This is due to the fact that these instabilities are driven by the strain field, thus their growth rates scale as the inverse of the square of the vortex separation.

Numerical calculations allow the approximations of the linear model to be relaxed, both for finite vortex-size effects and for the eventual fate of the instabilities. Nearly the same most-unstable wavenumbers are obtained as in the linear theory, even for the relatively closely spaced cases. These wavenumbers are in acceptable agreement with experiments considering uncertainties in measured vortex parameters, although some error may also be due to the non-ideal nature of the wake vortices.

For the co-rotating case, the long-term simulations resemble the experiments, and suggest a three-dimensional mechanism that allows merger to occur for a vortex pair too widely separated to do so in two dimensions. This process begins with a growing elliptic instability on at least one vortex, pushing peripheral vorticity beyond closed local streamlines. This vorticity then crosses over to the other vortex, forming an initial bridge between the two, which is in turn strained and intensified in the plane perpendicular to the vortex axis. The bridges increase in strength and the merger process continues until a single vortex remains.

The growth of the displacement instability of the counter-rotating case brings some sections of the weaker vortex in close proximity to the stronger one. These sections then wrap around the stronger vortex, leading to the formation of loops. This process continues, with the loops eventually forming rings which then self-induce away from the system and interact strongly with the other side of the wake.

R. L. Bristol and J. M. Ortega wish to thank the National Science Foundation for support from the Graduate Fellowship Program.

REFERENCES

- BAYLY, B. J. 1986 Three-dimensional instability of elliptical flow. *Phys. Rev. Lett.* **57**, 2160–2163.
- BRISTOL, R. L. 2000 Co-operative wake vortex instabilities. PhD Dissertation, University of California, Berkeley.
- BRISTOL, R. L., ORTEGA, J. M. & SAVAŞ, Ö. 1999 A towing tank study of airfoil wake vortices at Re of order 10^5 . *AIAA Paper* 99-3419.
- BRISTOL, R. L., ORTEGA, J. M. & SAVAŞ, Ö. 2003 Experimental study of corotating wake-vortex merger at Reynolds numbers of order 10^5 . *AIAA J.* **41**, 741–744.
- CHEN, A. L., JACOB, J. D. & SAVAŞ, Ö. 1999 Dynamics of corotating vortex pairs in the wakes of flapped airfoils. *J. Fluid Mech.* **383**, 155–193.
- CIFFONE, D. L. & ORLOFF, K. L. 1974 Axial flow measurements in trailing vortices. *AIAA J.* **12**, 1154–1155.
- CROUCH, J. D. 1997 Instability and transient growth for two trailing-vortex pairs. *J. Fluid Mech.* **350**, 311–330.
- CROUCH, J. D., MILLER, G. D. & SPALART, P. R. 2001 Active-control system for breakup of airplane trailing vortices. *AIAA J.* **39**, 2374–2381.
- CROW, S. C. 1970 Stability theory for a pair of trailing vortices. *AIAA J.* **8**, 2172–2179.
- DEVENPORT, W. J., VOGEL, C. M. & ZSOLDOS, J. S. 1999 Flow structure produced by the interaction and merger of a pair of corotating wing-tip vortices. *J. Fluid Mech.* **394**, 357–377.
- DURSTON, A. D., WALKER, W. S., DRIVER, D. M., SMITH, S. C. & SAVAŞ, Ö. 2004 Wake vortex alleviation flow field studies. *AIAA Paper* 2004-1073; also, accepted for publication in *J. Aircraft*.
- ELOY, C. & LE DIZES, S. 1999 Three-dimensional instability of Burgers and Lamb-Oseen vortices in a strain field. *J. Fluid Mech.* **378**, 145–166.
- FABRE, D. & JACQUIN, L. 2000 Stability of a four-vortex aircraft wake model. *Phys. Fluids* **12**, 2438–2443.

- FABRE, D., JACQUIN, L. & LOOF, A. 2002 Optimal perturbations in a four-vortex aircraft wake in counter-rotating configuration. *J. Fluid Mech.* **451**, 319–328.
- HAVERKAMP, S., NEUWERTH, G. & JACOB, D. 2003 Studies on the influence of outboard flaps on the vortex wake of a rectangular wing. *Aerospace Sci. Tech.* **7**, 331–339.
- JIMENEZ, J. 1975 Stability of a pair of corotating vortices. *Phys. Fluids* **18**, 1580–1581.
- KELVIN, LORD 1880 Vibrations of a columnar vortex. *Phil. Mag.* **10**, 155–168.
- KERSWELL, R. R. 2002 Elliptical instability. *Annu. Rev. Fluid Mech.* **34**, 83–113.
- KLEIN, R., MAJDA, A. J. & DAMODARAN, K. 1995 Simplified equations for the interaction of nearly parallel vortex filaments. *J. Fluid Mech.* **288**, 201–248.
- LE DIZÈS, S. & LAPORTE, F. 2002 Theoretical predictions for the elliptical instability in a two-vortex flow. *J. Fluid Mech.* **471**, 169–201.
- LESSEN, M., SINGH, P. & PAILLET, F. 1974 The stability of a line vortex. *J. Fluid Mech.* **63**, 753–763.
- LEWEKE, T. & WILLIAMSON, C. H. K. 1998 Cooperative elliptic instability of a vortex pair. *J. Fluid Mech.* **360**, 85–119.
- MARSHALL, J., BRANCHER, P. & GIOVANNINI, A. 2001 Interaction of unequal anti-parallel vortex tubes. *J. Fluid Mech.* **446**, 229–252.
- MATSUSHIMA, T. 1995 Spectral methods in polar coordinates with an application to the stability of a trailing vortex. PhD Dissertation, University of California, Berkeley.
- MATSUSHIMA, T. & MARCUS, P. S. 1995 A spectral method for polar coordinates. *J. Comput. Phys.* **120**, 365–374.
- MATSUSHIMA, T. & MARCUS, P. S. 1997 A spectral method for unbounded domains. *J. Comput. Phys.* **137**, 321–345.
- MOORE, D. W. & SAFFMAN, P. G. 1975 The instability of a straight vortex filament in a strain field. *Proc. R. Soc. Lond. A* **346**, 413–425.
- ORTEGA, J. M. 2001 Stability characteristics of counter-rotating vortex pairs in the wakes of triangular-flapped airfoils. PhD Dissertation, University of California, Berkeley.
- ORTEGA, J. M., BRISTOL, R. L. & SAVAŞ, Ö. 2002 Wake alleviation properties of triangular-flapped wings. *AIAA J.* **40**, 709–721.
- ORTEGA, J. M., BRISTOL, R. L. & SAVAŞ, Ö. 2003 Experimental study of the instability of unequal strength counter-rotating vortex pairs. *J. Fluid Mech.* **474**, 35–84.
- ORTEGA, J. M. & SAVAŞ, Ö. 2001 A rapidly growing instability mode in trailing multiple-vortex wakes. *AIAA J.* **39**, 750–754.
- PIERREHUMBERT, R. T. 1986 A universal short wave instability of two-dimensional eddies in an inviscid fluid. *Phys. Rev. Lett.* **57**, 2157–2159.
- PLOBECK, V. P. 1974 Stability calculations for rotating gas flows. MS Thesis, MIT.
- QUACKENBUSH, T. R., BILANIN, A. J., BATCHO, P. F., MCKILLIP, R. M., JR. & CARPENTER, B. F. 1997 Implementation of vortex wake control using SMA-actuated devices. In *Smart Structures and Materials 1997, Industrial and Commercial Applications of Smart Structure Technologies*, 4–6, March 1997. *Proc. SPIE Intl Soci. Optical Engng* **3044**, 134–146.
- RENNICH, S. C. & LELE, S. K. 1999 A method for accelerating the destruction of aircraft wake vortices. *J. Aircraft* **36**, 398–404.
- ROBINSON, A. C. & SAFFMAN, P. G. 1984 Three-dimensional stability of an elliptical vortex in a straining field. *J. Fluid Mech.* **142**, 451–466.
- ROSSOW, V. J. 1999 Lift-generated vortex wakes of subsonic transport aircraft. *Prog. Aerospace Sci.* **35**, 507–660.
- SAFFMAN, P. G. 1992 *Vortex Dynamics*. Cambridge University Press.
- SIPP, D. 2000 Weakly nonlinear saturation of short-wave instabilities in a strained Lamb-Oseen vortex. *Phys. Fluids* **12**, 1715–1729.
- TSAI, C. & WIDNALL, S. E. 1976 The stability of short-waves on a straight vortex filament in a weak externally imposed strain field. *J. Fluid Mech.* **73**, 721–733.
- WANG, H. 1998 short-wave instability on vortex filaments. *Phys. Rev. Lett.* **80**, 4665–4668.
- WIDNALL, S. E., BLISS, D. B. & TSAI, C.-Y. 1974 The instability of short-waves on a vortex ring. *J. Fluid Mech.* **66**, 35–47.
- WIDNALL, S. E., BLISS, D. B. & ZALAY, A. 1971 Theoretical and experimental study of the stability of a vortex pair. In *Aircraft Wake Turbulence and Its Detection*, pp. 305–338. Plenum.